

Constraining neutrino masses with weak-lensing starlet peak counts

Virginia Ajani,^{1,*} Austin Peel,² Valeria Pettorino,¹ Jean-Luc Starck,¹ Zack Li,³ and Jia Liu^{4,3}

¹*AIM, CEA, CNRS, Université Paris-Saclay, Université Paris Diderot,
Sorbonne Paris Cité, F-91191 Gif-sur-Yvette, France*

²*Laboratoire d'Astrophysique, Ecole Polytechnique Fédérale de Lausanne (EPFL),
Observatoire de Sauverny, CH-1290 Versoix, Switzerland*

³*Department of Astrophysical Sciences, Princeton University, 4 Ivy Lane, Princeton, NJ 08544, USA*

⁴*Berkeley Center for Cosmological Physics, University of California, Berkeley, CA 94720, USA*

Massive neutrinos influence the background evolution of the Universe as well as the growth of structure. Being able to model this effect and constrain the sum of their masses is one of the key challenges in modern cosmology. Weak gravitational lensing by the large-scale structure has proven to be a powerful tool to achieve this goal, and its importance to precision cosmology is borne out in the scientific results of galaxy surveys such as the Canada-France-Hawaii Telescope Lensing Survey (CFHTLenS), the Kilo-Degree Survey (KiDS), the Dark Energy Survey (DES) and Hyper SuprimeCam (HSC). Weak-lensing cosmological constraints will also soon reach higher levels of precision with next-generation surveys like LSST, WFIRST and *Euclid*. In this context, we use the *MassiveNus* simulations to derive constraints on the sum of neutrino masses M_ν , the present-day total matter density Ω_m , and the primordial power spectrum normalization A_s in a tomographic setting. Along with the lensing power spectrum, we use peak counts as higher-order statistics. We find that the combination of the two statistics does not add any relevant information over considering just the peaks alone. We also compare two different filtering techniques on noisy maps and show that a starlet (wavelet) filter produces tighter constraints than Gaussian filtering by 50%, 25%, and 38% on M_ν , Ω_m , and A_s , respectively. For the starlet case, we further find a minimum resolution that allows us to obtain constraints comparable to what is achieved with the full wavelet decomposition, and we show that the information contained in the coarse map cannot be neglected.

I. INTRODUCTION

The presence of massive neutrinos affects the background evolution of the Universe as well as the evolution of cosmological perturbations and structure formation [1]. Constraining the value of the sum of neutrino masses is one of the key science goals of modern cosmology. This is not only an interesting goal per se, but it is also worth exploring because in the presence of massive neutrinos, modified gravity models may mimic the standard cosmological (Λ CDM) model, as discussed in [2–4]. This is due to the fact that massive neutrinos modify structure formation, typically reducing clustering, and can therefore allow for larger non-standard couplings than in the absence of massive neutrinos. Being able to measure massive neutrinos can also allow us to disentangle Λ CDM from alternative scenarios. From neutrino oscillation experiments, [5] we only have information about the difference of the masses squared. Hence, to fix a scale for the neutrino masses, it is necessary to assume a mass hierarchy: for a *normal* hierarchy (*i.e.* $m_1 < m_2 < m_3$) the lower bound on the sum of neutrino masses $M_\nu \equiv \sum_\nu m_\nu$ is currently predicted to be $M_\nu > 0.06$ eV while for an *inverted* hierarchy (*i.e.* $m_3 < m_1 < m_2$) $M_\nu > 0.1$ eV [6]. The latest results on the upper bound have been obtained by combining the Cosmic Microwave Background (CMB) temperature fluctuation data with CMB lensing and Baryon Acoustic Oscillations (BAO), leading to a

constraint of $M_\nu < 0.12$ eV at 95% confidence level [7].

Weak gravitational lensing by large-scale structure encodes the evolution of structure growth under the influence of massive neutrinos, representing a powerful tool to explore these effects and extract the corresponding cosmological information. Future galaxy surveys like *Euclid* [8] will be sensitive to the properties of weakly interacting particles in the eV mass range, such as massive neutrinos, and will use weak lensing as a cosmological probe to test different models and improve our knowledge of cosmological parameters.

Moreover, in recent years, it has been shown that weak-lensing statistics higher than second order can help break degeneracies, as they take into account the non-Gaussian information encoded by the non-linear process of structure formation, such as the bispectrum [9, 10], Minkowski functionals [11, 12], and peak counts [13–18]. In this context, we perform Bayesian inference to derive cosmological constraints on the sum of neutrino masses M_ν , the matter density parameter Ω_m , and the primordial power spectrum amplitude A_s , for a survey with *Euclid*-like noise. We use as synthetic data the lensing convergence maps from *MassiveNus* simulations [19, 20]. Using the same suite of simulations, [21], [22], and [23] have already shown for a LSST-like survey [24] that combining the lensing power spectrum with higher-order statistics can provide tighter constraints on parameters. For this purpose, we perform our analysis using the lensing power spectrum and peak counts as summary statistics following [25]. We extend the study by considering a survey with *Euclid*-like noise, and to smooth the noisy convergence maps we employ a starlet filter [26], which

* virginia.ajani@cea.fr

was shown to be a powerful tool in the context of weak-lensing peak counts by [27].

The paper is organised as follows: [section II](#) describes the theoretical framework of weak gravitational lensing useful for the paper and the simulations we use. Then, we illustrate the survey and noise settings, the filtering techniques that we employ for the comparison and the details of the summary statistics. In [section III](#) we describe the interpolation method implemented to build the likelihood, the covariance matrices, the results estimators that we employ to quantify our results and the settings of the MCMC. The cosmological parameter constraints are shown in [section IV](#). We conclude in [section V](#).

II. METHODOLOGY

A. Weak lensing

The effect of gravitational lensing at comoving angular distance $f_K(\chi)$ can be described by the *lensing potential*

$$\psi(\vec{\theta}, \chi) \equiv \frac{2}{c^2} \int_0^\chi d\chi' \frac{f_K(\chi - \chi')}{f_K(\chi)f_K(\chi')} \Phi(f_K(\chi')\vec{\theta}, \chi'), \quad (1)$$

which defines how much the gravitational potential Φ arising from a mass distribution changes the direction of a light path. In this expression K is the spatial curvature constant, χ is the comoving radial coordinate, $\vec{\theta}$ is the angle of observation, and c is the speed of light. As we are in Λ CDM, the two Bardeen gravitational potentials are here assumed to be equal and the metric signature is defined as $(+1, -1, -1, -1)$. In particular, under the *Born approximation* the effect of the lensing potential on the shapes of background galaxies in the weak regime can be summarised by its variation with respect to $\vec{\theta}$. Formally, this effect can be described by the elements of the lensing potential Jacobi matrix:

$$A_{ij} = \delta_{ij} - \partial_i \partial_j \psi, \quad (2)$$

which can be parametrised as

$$A = \begin{pmatrix} 1 - \kappa - \gamma_1 & -\gamma_2 \\ -\gamma_2 & 1 - \kappa + \gamma_1 \end{pmatrix}, \quad (3)$$

where (γ_1, γ_2) are the components of a spin-2 field γ called *shear*, and κ is a scalar quantity called *convergence*. They describe respectively the anisotropic stretching and the isotropic magnification of the galaxy shape when light passes through large-scale structure. [Equation 2](#) and [Equation 3](#) define the shear and the convergence fields as second-order derivatives of the lensing potential:

$$\gamma_1 \equiv (\partial_1 \partial_1 - \partial_2 \partial_2) \psi \quad \gamma_2 \equiv \partial_1 \partial_2 \psi \quad (4)$$

$$\kappa \equiv \frac{1}{2} (\partial_1 \partial_1 + \partial_2 \partial_2) \psi = \frac{1}{2} \nabla^2 \psi. \quad (5)$$

The weak-lensing field is a powerful tool for cosmological inference. The shear is more closely related to actual observables (i.e., galaxy shapes), while the convergence, as a scalar field, can be more directly understood in terms of the matter density distribution along the line of sight. This can be seen by inserting the lensing potential defined in [Equation 1](#) inside [Equation 5](#) and using the fact that the gravitational potential Φ is related to the matter density contrast $\delta = \Delta\rho/\bar{\rho}$ through the Poisson equation $\nabla^2 \Phi = 4\pi G a^2 \bar{\rho} \delta$. Expressing the mean matter density in terms of the critical density $\rho_{c,0} = 3H_0^2/(8\pi G)$, the convergence field can be rewritten as

$$\kappa(\vec{\theta}) = \frac{3H_0^2 \Omega_m}{2c^2} \int_0^{\chi_{\text{lim}}} \frac{d\chi}{a(\chi)} g(\chi) f_K(\chi) \delta(f_K(\chi)\vec{\theta}, \chi), \quad (6)$$

where H_0 is the Hubble parameter at its present value, and

$$g(\chi) \equiv \int_\chi^{\chi_{\text{lim}}} d\chi' n(\chi') \frac{f_K(\chi' - \chi)}{f_K(\chi')} \quad (7)$$

is the *lensing efficiency*. [Equation 6](#) relates the convergence κ to the 3D matter overdensity field $\delta(f_K(\chi)\vec{\theta}, \chi)$, and it describes how the lensing effect on the matter density distribution is quantified by the lensing strength at a distance χ that directly depends on the normalised source galaxy distribution $n(z)dz = n(\chi)d\chi$ and on the geometry of the universe through $f_K(\chi)$ along the line of sight. For a complete derivation see [28] and [29].

B. Simulations

In this paper, we use the Cosmological Massive Neutrino Simulations ([MassiveNus](#)), a suite of publicly available N-body simulations released by the Columbia Lensing group¹. It contains 101 different cosmological models obtained by varying the sum of neutrino masses M_ν , the total matter density parameter Ω_m and the primordial power spectrum amplitude A_s at the pivot scale $k_0 = 0.05 \text{ Mpc}^{-1}$, in the range $M_\nu = [0, 0.62] \text{ eV}$, $\Omega_m = [0.18, 0.42]$ and $A_s \cdot 10^9 = [1.29, 2.91]$. The reduced Hubble constant $h = 0.7$, the spectral index $n_s = 0.97$, the baryon density parameter $\Omega_b = 0.046$ and the dark energy equation of state parameter $w = -1$ are kept fixed under the assumption of a flat universe. The fiducial model is set at $\{M_\nu, \Omega_m, 10^9 A_s\} = \{0.1, 0.3, 2.1\}$.

The presence of massive neutrinos is taken into account assuming normal hierarchy and using a linear response method, where the evolution of neutrinos is described by linear perturbation theory but the clustering occurs in a non-linear cold dark matter potential.

¹ <http://columbialensing.org>

The simulations have a 512 Mpc/h box size with 1024^3 CDM particles. They are implemented using a modified version of the public tree-Particle Mesh (tree-PM) code **Gadget2** with a neutrino patch, describing the impact of massive neutrinos on the growth of structures up to $k = 10 \text{ h Mpc}^{-1}$. For a complete description of the implementation and the products see [20]. We use the simulated convergence maps as mock data for our analysis. When dealing with real data the actual observable is the shear field that can be converted into the convergence field following [30]. We bypass this step from γ to κ and work with the convergence maps directly provided as products from **MassiveNus**. The maps are generated using the public ray-tracing package **LensTools** [19] for each of the 101 cosmological models at five redshifts $z = \{0.5, 1.0, 1.5, 2.0, 2.5\}$. Each redshift has 10000 different map realisations obtained by rotating and shifting the spatial planes. Each κ map has 512^2 pixels, corresponding to a 12.25 deg^2 total angular size area in the range $\ell \in [100, 37000]$ with a resolution of 0.4 arcmin.

C. Noise and survey specifications

The method described in this paper can be applied to any given survey. For illustration purposes, we perform here a tomographic study using redshifts $z = \{0.5, 1.0, 1.5, 2.0\}$ and mimicking the noise expected for a survey like *Euclid*²[8, 31]. Specifically, at each redshift we produce 10000 map realisations of Gaussian noise with mean zero and variance

$$\sigma_n^2 = \frac{\langle \sigma_\epsilon^2 \rangle}{n_{\text{gal}} A_{\text{pix}}}, \quad (8)$$

where we set the dispersion of the ellipticity distribution to $\sigma_\epsilon = 0.3$, and the pixel area is given by $A_{\text{pix}} \simeq 0.16 \text{ arcmin}^2$. The redshift dependence that makes a tomographic investigation possible is encoded in the source galaxy redshift distribution, for which we assume the parametric form

$$n(z) = \mathcal{C} \left(\frac{z}{z_0} \right)^\alpha \exp \left[- \left(\frac{z}{z_0} \right)^\beta \right], \quad (9)$$

with $\alpha = 2$, $\beta = 3/2$, $z_0 = 0.9/\sqrt{2}$ as in [8, 31], and \mathcal{C} is the normalization constant to guarantee the constraint $\int_{z_{\text{min}}}^{z_{\text{max}}} n(z) dz = 30 \text{ arcmin}^{-2}$. Then, we compute the galaxy number density at each bin as

$$n_{\text{gal}}^i = \mathcal{C} \int_{z_i^-}^{z_i^+} n(z) dz, \quad (10)$$

where z_i^-, z_i^+ are the edges of the i^{th} bin. We adapt the binning choice to the provided simulation settings,

assuming that we observe galaxies within a small range around the actual redshift. This leads to the values for the galaxy number density n_{gal} per source redshift bin z_s provided in Table I:

z_s	0.5	1.0	1.5	2.0
n_{gal}	11.02	11.90	5.45	1.45

TABLE I. Values of n_{gal} for each source redshift z_s . We adapt the binning choice to the provided simulation settings, assuming that we observe galaxies within a small range around the actual redshift. In practice, this means considering as bin edges $\{0.001, 0.75, 1.25, 1.75, 2.25\}$, in order to compute the integral in Equation 10.

D. Gaussian and starlet filters

In order to access the signal in the convergence maps at small scales (where they are mostly dominated by noise), we filter them, considering and comparing two different techniques. First, we use a Gaussian kernel of size θ_{ker} , defined as

$$\mathcal{G}(\theta/\theta_{\text{ker}}) = \frac{1}{\sqrt{2\pi}\theta/\theta_{\text{ker}}} e^{-\theta/\theta_{\text{ker}}^2}, \quad (11)$$

which was also used in e.g. [25, 32]. We then compare results with those obtained when applying instead an *Isotropic Undecimated Wavelet Transform*, also known as a starlet transform [33], which allows us to represent an image I as a sum of wavelet scales images w_j and a coarse resolution image c_J . The starlet filter is a wavelet transform, i.e. a function satisfying the *admissibility condition* that allows for the simultaneous processing of data at different scales. An original map I is decomposed by this transform into a coarse version of it c_J plus several images of the same size at different resolution scales j :

$$I(x, y) = c_J(x, y) + \sum_j^{j_{\text{max}}} w_j(x, y), \quad (12)$$

where wavelet images w_j represent the details of the original image at dyadic scales corresponding to a spatial size of 2^j pixels and $J = j_{\text{max}} + 1$. The starlet wavelet function ψ is derived from a B-spline function ϕ of order 3:

$$\psi(t_1, t_2) = 4\phi(2t_1, 2t_2) - \phi(t_1, t_2) \quad (13)$$

with

$$\phi(t) = \frac{1}{12} (|t-2|^3 - 4|t-1|^3 + 6|t|^3 - 4|t+1|^3 + |t+2|^3) \quad (14)$$

and $\phi(t, t') = \phi(t)\phi(t')$. For a complete description and derivation of the starlet transform algorithm, see [26].

² <https://www.Euclid-ec.org>

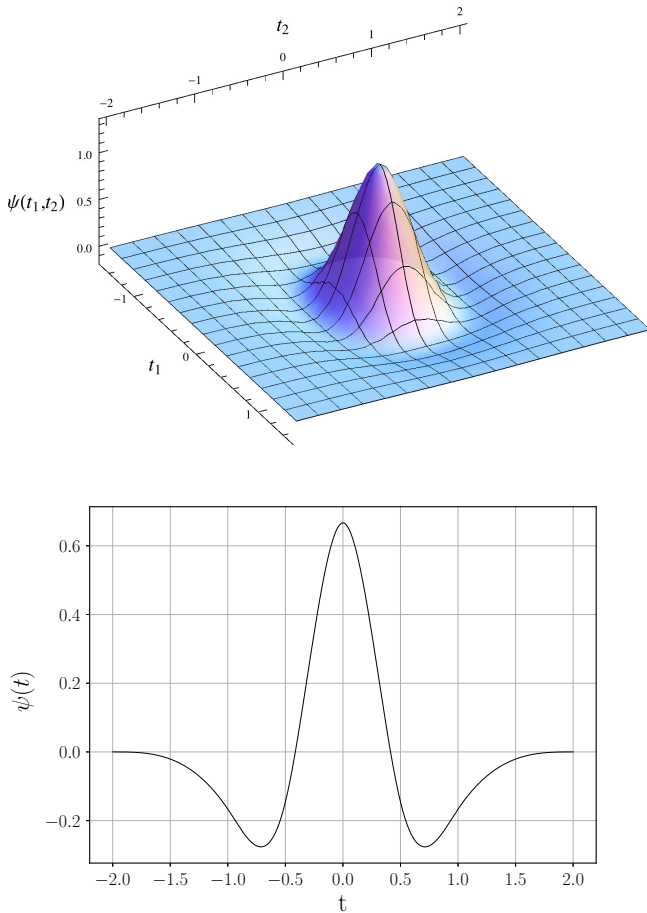


FIG. 1. We show the 2D starlet function (top panel) as defined in Equation 13 and its 1D profile (bottom panel). Being a wavelet it is a compensated function, i.e. it integrates to zero over its domain. This comes from the *admissibility condition* for the wavelet function ψ : $\int_0^{+\infty} |\psi(k)|^2 \frac{dk}{k} < +\infty$ which implies that $\int \psi(x) dx = 0$ and it has compact support in $[-2, 2] \times [-2, 2]$. Its shape emphasises round features, making it very efficient when dealing with peaks.

One of the advantages of employing a starlet filter is provided by its multi-scale analysis, namely its ability to investigate and extract the information encoded at different scales at the same time [34]. Hence, the starlet transform presents the properties to compute efficiently J scales with a fast algorithm with a complexity of $\mathcal{O}(N^2 \log N)$ for an image of $N \times N$ pixels and to analyse data with compensated aperture filters with finite support. See also [15, 35] for further details on the advantages of wavelet starlet analysis. The following example illustrates how we can compare results from these two different filtering schemes. Applying a starlet transform with $j_{max} = 4$ to a map with 0.4 arcmin pixel size will result in a decomposition of four maps with resolutions [0.8, 1.6, 3.2, 6.4] arcmin plus the coarse map. For our study, we will consider as finest scale $\theta_{ker} = 1.6$ arcmin, being a more realistic choice in terms of resolution for convergence maps coming from *Euclid*-like survey data. We will therefore focus

on the set of scales [1.6, 3.2, 6.4] arcmin plus the coarse map. To fairly compare the two filters, we then choose the smoothing size for the Gaussian kernel such that it encodes all the information provided by the starlet that will correspond to the finest scale (in this case $\theta_{ker} = 1.6$ arcmin). The corresponding Fourier space response for each individual starlet scale and for the Gaussian kernel is depicted in Figure 2.

Based on the above, in our study we compare cosmological constraints obtained using noisy maps smoothed with a Gaussian kernel of $\theta_{ker} = 1.6$ arcmin with the ones obtained from a starlet decomposition of the same maps up to $\theta_{ker} = 1.6$ arcmin. We exclude the observables corresponding to 0.8 arcmin in our analysis after having verified that this does not cost any loss of information. In Figure 3 we show the result of the filtering procedure for a Gaussian kernel: given the original convergence map κ , we add white noise as described in section II C and then we filter the noisy map with the chosen kernel.

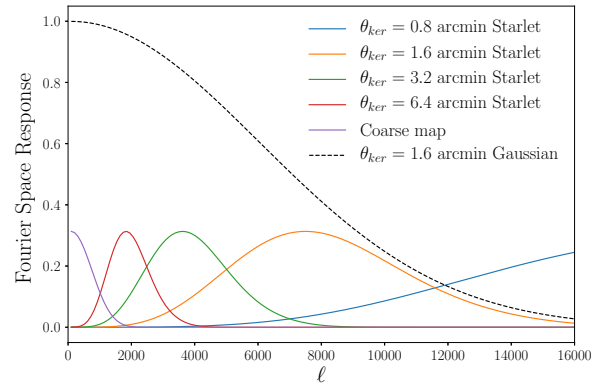


FIG. 2. Fourier response of starlet and Gaussian filter in Fourier Space as a function of $\ell = (2\pi \text{ pixel}) / (\text{map size})$. The coloured lines show the response in Fourier space of the starlet decomposition. Specifically: the finest scale (highest frequency) is the blue line and corresponds to 0.8 arcmin for a map with pixel size = 0.4 arcmin. The following term in the decomposition is given by the orange line, equivalent to 1.6 arcmin and so on for powers of two. The last term of the starlet decomposition is the *coarse* map (violet line), which is a smooth version of the original map, namely $c_J(x, y)$ in Equation II D. The dashed black line represents a Gaussian kernel as defined in Equation II D with $\theta_{ker} = 1.6$ arcmin.

E. Summary statistics

To extract and investigate the cosmological information encoded in the weak lensing convergence maps, we compute the power spectrum (PS) and peak counts as summary statistics.

1. Convergence power spectrum

To provide a statistical estimate of the distribution of the convergence field, the first non-zero order is given by its second moment, which is commonly described by the *two-point correlation function* (2PCF) in real space $\langle \kappa(\theta)\kappa(\theta') \rangle$, or by its counterpart in Fourier space, the *convergence power spectrum*:

$$C_\kappa(\ell) = \frac{9\Omega_m^2 H_0^4}{4c^4} \int_0^{\chi_{\text{lim}}} d\chi \frac{g^2(\chi)}{a^2(\chi)} P_\delta\left(\frac{\ell}{f_\kappa(\chi)}, \chi\right) \quad (15)$$

where P_δ represents the 3D matter power spectrum, directly related to the matter density distribution δ in Equation 6 of the weak-lensing convergence field. In this study, we compute the power spectrum of the noisy filtered convergence maps: for a given cosmology we add Gaussian noise to each realisation of κ . For each redshift we generate a different set of noise maps following Equation 8.

To filter the maps we employ a Gaussian kernel with smoothing size $\theta_{\text{ker}} = 1$ arcmin and consider angular scales with logarithmically spaced bins in the range $\ell = [300, 5000]$. We compute the power spectra using *LensTools* for each of the 10000 realisations per cosmology and then we take the average over the realisations. We parallelise our code using *joblib*³ to accelerate processing due to the large number of realisations per cosmology.

2. Peak counts

Second order statistics such as the power spectrum have been widely used in studies performing cosmological parameter estimation with cosmic shear; see, for example, [36–38]. However, it is well known that it is necessary to go beyond second-order statistics in order not to lose the non-Gaussian information in the matter distribution due to the weak-lensing correlations arising in the non-linear regime. Recently, several studies have considered weak-lensing peak counts as a robust and complementary probe to the power spectrum to constrain cosmological parameters [13–18, 25, 27]. **The physical meaning of weak lensing peaks can be identified in the fact that they trace regions where the value of the convergence field is high, hence, they are in some way associated to massive structures.** Nevertheless, their exact relation with halos is not trivial due to projection and noise that can generate false detections.

In this paper, we detect and count weak lensing peaks on the noisy filtered maps using our own code⁴. We compute peaks as local maxima of the signal-to-noise field ν

i.e. as a pixel of larger value than its eight neighbors in the image. We define the signal to noise field $\nu = S/N$ as the ratio between the noisy convergence κ convolved with the filter $\mathcal{W}(\theta_{\text{ker}})$ over the smoothed standard deviation of the noise for each realisation per redshift:

$$\nu = \frac{(\kappa * \mathcal{W})(\theta_{\text{ker}})}{\sigma_n^{\text{filt}}}, \quad (16)$$

where $\mathcal{W}(\theta_{\text{ker}})$ can be the Gaussian or the starlet filter. Concerning σ_n^{filt} , its definition depends on the employed filter. For a Gaussian kernel it is given by the standard deviation of the smoothed noise maps, while for the starlet case we need to estimate the noise at each wavelet scale for each image per redshift. To estimate the noise level at each starlet scale we follow [39] and use the fact that the standard deviation of the noise at the scale j is given by $\sigma_j = \sigma_j^e \sigma_I$, where σ_I is the standard deviation of the noise of the image and σ_j^e are the coefficients obtained by taking the standard deviation of the starlet transform of a Gaussian distribution with standard deviation one at each scale j . To estimate σ_I we take the *median absolute deviation*⁵ of the noisy convergence map. We do this for each one of the 10000 realisations for each cosmology and then take the average over the realisations. We consider the peak distribution for 50 linearly spaced bins within the range $\nu = [-0.6, 6]$.

III. ANALYSIS

A. Likelihood

To perform Bayesian inference and get the probability distributions of the cosmological parameters, we use a Gaussian likelihood for a cosmology-independent covariance:

$$\log \mathcal{L}(\theta) = \frac{1}{2} (d - \mu(\theta))^T C^{-1} (d - \mu(\theta)), \quad (17)$$

where d is the data array, C is the covariance matrix of the observables, μ the expected theoretical prediction as a function of the cosmological parameters θ . In our case, the data array is the mean over the (simulated) realisations of the power spectrum or peak counts or combination of the two for our fiducial model. Cosmological parameters are the ones for which simulations are available, i.e. $\{M_\nu, \Omega_m, A_s\}$.

³ <https://joblib.readthedocs.io/>

⁴ Code publicly available at <https://github.com/CosmoStat/lenspack>

⁵ For a Gaussian distribution the *median absolute deviation* (MAD) and the standard deviation are directly related as: $\text{MAD}/\sigma = 0.6745$. We choose to use this estimator since it is more robust when dealing with non-normal distributions (being more resistant to outliers in a data set) to have a more general implementation in our pipeline.

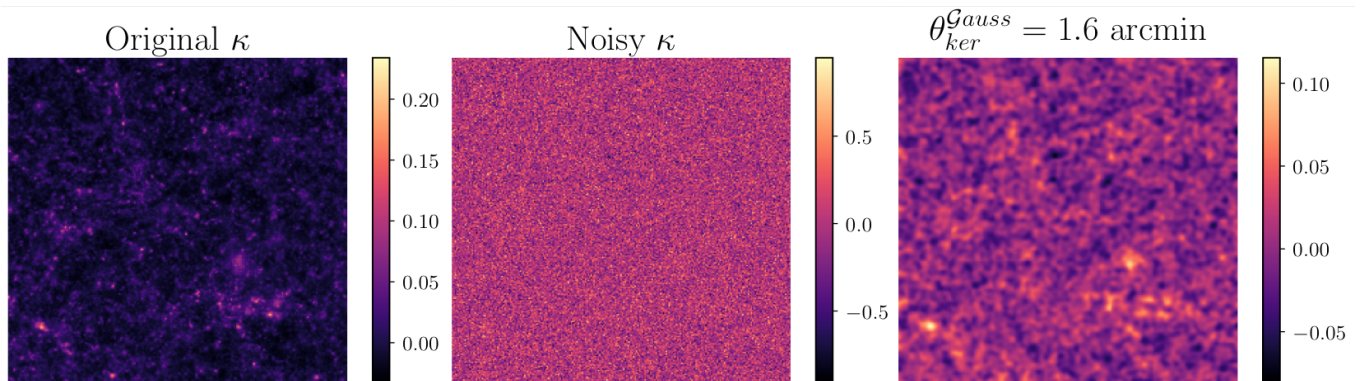


FIG. 3. Convergence maps κ are noiseless. We apply Gaussian noise and then filter the map using either the Gaussian or starlet filtering. For illustration purposes, we show the Gaussian filtering with $\theta_{ker}^{Gauss} = 1.6$ arcmin of one map realisation for the fiducial model $\{M_\nu, \Omega_m, 10^9 A_s\} = \{0.1, 0.3, 2.1\}$. The color bar on the right of each map describes values of the convergence field κ . For each realisation of the 10000 maps provided for each redshift we generate 10000 noise maps as described in section II C corresponding to the different value of n_{gal} respectively for $z=[0.5, 1.0, 1.5, 2.0]$.

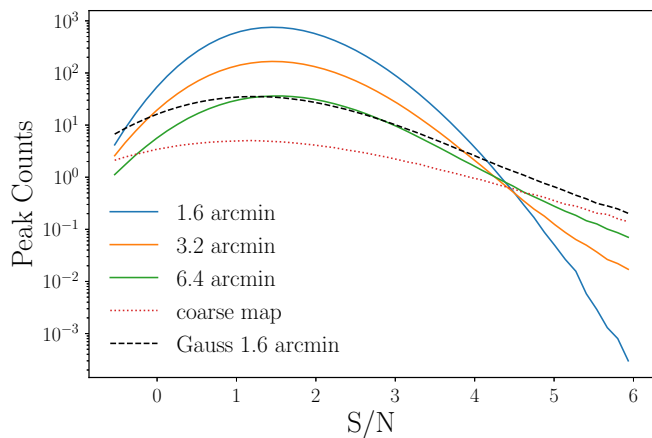


FIG. 4. Peak Counts distribution in logarithmic scale for each starlet scales resolutions: [1.6, 3.2, 6.4] arcmin and the coarse maps (red dotted line) and the Gaussian case (black dashed line). Due to the decomposition at different scales, for each map filtered with the starlet there are 4 different distributions. Indeed, the number of counts depends on the resolution: the larger the smoothing size (the lower the frequency) the smaller the number of peaks.

In order to determine the relation between the observables and the models $\mu(\theta)$, i.e. to be able to have a prediction of the power spectrum and the peak counts given a new set of cosmological parameters $\{M_\nu, \Omega_m, A_s\}$, we employ an interpolation with Gaussian Processes Regression (GPR, [40]) using the `scikit-learn` python package. Gaussian Processes are a generic supervised learning method that, via an assumption of smoothness between parameters with close values, allows one to compute the prediction for an observable at a new given point in parameter space. The cosmological parameters and the corresponding observables (power spectrum and peak counts or the two statistics combined) from the simulations are used as a training set, i.e. as the input for the GPR.

Then, the Gaussian Processes act by assuming that for a new point in parameter space θ_* which is sufficiently close to a known point θ belonging to the training set, the corresponding observable will be described by a joint normal distribution along with the known observable. This can be summarised by:

$$\begin{bmatrix} f \\ f_* \end{bmatrix} \sim \mathcal{N} \left(\begin{bmatrix} \mu \\ \mu_* \end{bmatrix}, \begin{bmatrix} K(\theta, \theta) + \sigma_n^2 I & K(\theta, \theta_*) \\ K(\theta_*, \theta) & K(\theta_*, \theta_*) \end{bmatrix} \right),$$

where $K(\theta, \theta')$ is the *kernel* of the Gaussian processes that assesses the smooth relation among points in parameter space and has form of an *anisotropic squared exponential* function. σ_n is the standard error of the noise level in the targets, namely in our case the noise given by the fact that we take the mean over 10000 realisations for each observable and each bin. For the validation we use the *leave-one-out* cross-validation for which the training set is given by all the samples except one, and the test set is the sample left out.

B. Covariance matrices

We use the independent fiducial massless simulation, defined by $\{M_\nu, \Omega_m, 10^9 A_s\} = \{0.0, 0.3, 2.1\}$ and obtained from initial conditions different from the massive simulations to compute the covariance matrices of the data. We consider a parameter-independent covariance to reduce the risk of assigning an excess of information to the observables in the context of a Gaussian likelihood assumption, following the results of [41]. The covariance matrix elements are computed as

$$C_{ij} = \sum_{r=1}^N \frac{(x_i^r - \mu_i)(x_j^r - \mu_j)}{N-1} \quad (18)$$

where N is the number of observations (in this case the 10000 realizations), x_i^r is the value of the power spectrum or the peak counts in the i^{th} bin for a given realisation r and

$$\mu_i = \frac{1}{N} \sum_r x_i^r \quad (19)$$

is the mean of the power spectrum or the peak counts in a given bin over all the realisations. In Figure 5 we show the correlation coefficients of the observable corresponding to the combination of the power spectrum (bins 1-24) and the starlet peak counts (bins 75-224) for $z = 1$. Notice that since we perform a tomographic analysis, the covariance that will be implemented in the likelihood is a concatenation of power spectrum arrays for each redshift and a concatenation of peak counts for each redshift. In the case of the starlet, this means that for each redshift there are 4 different (starlet) scales, each one with 50 bins in values of signal to noise.

Furthermore, we take into account the loss of information due to the finite number of bins and realisations by adopting for the inverse of the covariance matrix the estimator introduced by [42]:

$$C^{-1} = \frac{N - n_{\text{bins}} - 2}{N - 1} C_*^{-1}, \quad (20)$$

where N is the number of realisations, n_{bins} the number of bins, and C_* the covariance matrix computed for the power spectrum and peak counts. **We also scale the covariance for a *Euclid* sky coverage by the factor $f_{\text{map}}/f_{\text{survey}}$, where $f_{\text{map}} = 12.25 \text{ deg}^2$ the size of the convergence maps and $f_{\text{Euclid}} = 15000 \text{ deg}^2$.** In using Equation 20, we do not expect all biases to be removed from our parameter inference, as this has already been ruled out in [43] and [44]. Nevertheless, we rely on the fact that the number of realisations that we are using (10000) is sufficiently large and greater than n_{bins} to consider it a reliable estimator for our case ⁶.

C. Result estimators

In order to quantify our results, we use estimators common in the literature, whose definitions we recall here for convenience.

1. Figure of Merit

To have an approximate quantification of the size of the parameter contours that we use to compare their con-

⁶ Indeed, the value of the correction coefficient is close to 1 for each analysis we perform. However, considering that the results of [44] quantify the loss of information also in the case of a *Euclid*-like survey, it would be worth it to reproduce our study applying their restoration technique to generalize our analysis.

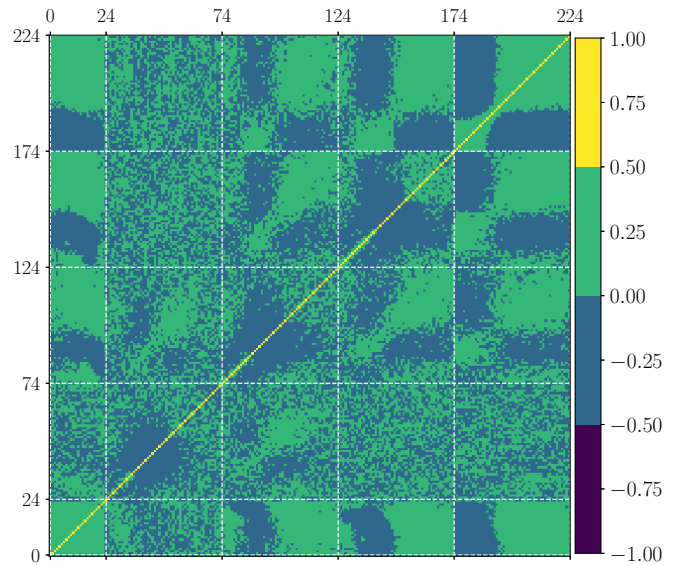


FIG. 5. Starlet filtering, redshift $z=1$ correlation matrix for the observables. Bins 1-24: noisy power spectrum, bins 25-74: peak counts for 1.6 arcmin, bins 74-124: peak counts for 3.2 arcmin. Bins 124-174: peak counts for 6.4 arcmin. Bins 174-224: peak counts for the coarse map.

straining power, we consider the following Figure of Merit (FoM) as defined in [31]:

$$\text{FoM}_{\alpha\beta} = \sqrt{\det(\tilde{F}_{\alpha\beta})} \quad (21)$$

where α and β are pairs of parameters from the set $\{M_\nu, \Omega_m, 10^9 A_s\}$, and $\tilde{F}_{\alpha\beta}$ is the marginalised Fisher submatrix that we estimate as the inverse of the covariance matrix $C_{\alpha\beta}$ of the cosmological parameters obtained with the MCMC chains.

2. Figure of correlation

To quantify the correlations among the parameters we use the *Figure of Correlation* [31, 45]:

$$\text{FoC} = \sqrt{\det(\mathbf{P}^{-1})}, \quad (22)$$

where \mathbf{P} is the correlation matrix whose elements are defined as $P_{\alpha\beta} = C_{\alpha\beta} / \sqrt{C_{\alpha\alpha} C_{\beta\beta}}$, with $C_{\alpha\beta}$ the covariance between the cosmological parameters α and β as defined in the previous section. When the parameters are fully uncorrelated $\text{FoC} = 1$, while for $\text{FoC} > 1$ the off-diagonal terms are non-zero, indicating an increasing presence of correlations among parameters as FoC increases. The values of the FoC for our constraints are shown in Table IV and we will comment on them in section IV.

Condition Number	PS	Gaussian Peaks	Starlet Peaks
Tomo $z = [0.5 - 2.0]$	10^7	10^5	10^{16}
Single $z = 1$	10^5	10^3	10^6

TABLE II. Values of the Condition Number for the data covariance matrices. The smaller the number the easier it is to invert the matrix. In this case we get very large values for this estimator, leading to the conclusion that the data covariance matrices for all the three probes - PS, Starlet Peaks and Gaussian Peaks - show very singular behaviour.

3. Matrix condition number

To estimate how difficult it is to invert our data covariance matrices, we compute the corresponding *condition number*: if the matrix is singular, the associated condition number is infinite, i.e. matrices with large condition numbers are more difficult to invert. We compute the condition number through the 2-norm of the matrix using singular value decomposition (SVD). As shown in Table II, the condition numbers of the tomographic case, both with the starlet and the Gaussian kernels are characterised by very high values. Indeed, we find that the corresponding covariance matrices exhibit singular values, especially for redshift $z = 0.5$ and $z = 2.0$. To overcome this issue and to perform parameter inference when inverting the covariance matrix in Equation 17, we consider the *Moore-Penrose* pseudo-inverse of the matrix. This makes the computation of the generalized inverse of the covariance matrix possible by using its SVD and including all large singular values.

D. MCMC simulations and posterior distributions

To explore and constrain the parameter space, we use the `emcee` package, which is a python implementation of the affine-invariant ensemble sampler for Markov chain Monte Carlo (MCMC) introduced by [?]. The pipeline is built in a way that both the computation of the power spectrum and peak counts along with the MCMC are run in parallel to gain computation time. We assume a flat prior, specifically following [23], a Gaussian likelihood function as defined in Equation 17, and a model-independent covariance matrix as discussed in section III B. The walkers are initialised in a tiny Gaussian ball of radius 10^{-3} around the fiducial cosmology $[M_\nu, \Omega_m, 10^9 A_s] = [0.1, 0.3, 2.1]$ and we estimate the posterior using 200 walkers. To plot the contours we use the `ChainConsumer` python package [47].

IV. RESULTS

We now illustrate forecast results on the sum of neutrino masses M_ν , on the matter density parameter Ω_m and on the power spectrum amplitude A_s for a survey with *Euclid*-like noise in a tomographic setting with four

source redshifts $z = [0.5, 1.0, 1.5, 2.0]$, and compare results for different observables (power spectrum and peak counts) and filters (Gaussian and starlet).

A. Gaussian vs starlet peak counts

In the left panel of Figure 6 we compare constraints obtained from the power spectrum (blue contours), the peak counts of noisy maps smoothed with a Gaussian kernel (green contours) and the peak counts of noisy maps smoothed with a starlet kernel (red contours). We confirm that peak counts outperform power spectrum constraints as found in [25]. In addition, we find that employing a starlet filter instead of a Gaussian one - with a smoothing size that corresponds to the finest starlet scale - leads to tighter constraints. We quantify these outcomes by considering the Figure of Merit defined in Equation 21. As shown in Table III, the FoM for the Gaussian peaks relative to the parameter space plane (M_ν, Ω_m) is more than three times the one given by the power spectrum and the one from starlet peaks is more than twice the one obtained with the Gaussian peaks. Concerning the (M_ν, A_s) and (Ω_m, A_s) planes, the Gaussian peaks FoM is about four times the one given by the power spectrum and the one from starlet peaks is again about twice the one obtained with the Gaussian peaks (and more than eight times the power spectrum FoM). As further investigation, we compute the Figure of Correlation as defined in Equation 22 to study the correlation among the parameters. By looking at Table IV, one can see how values for the power spectrum for the pairs (M_ν, Ω_m) and (Ω_m, A_s) are close to one, suggesting that correlation among them appears to be very small. Correlation between (M_ν, A_s) , as its FoC is nearly twice as large. Qualitatively this can be appreciated by looking at the inclination of the contours. More specifically, concerning the plane (M_ν, Ω_m) , the power spectrum contours are horizontal and show also visually that these two parameters are not correlated; constraints obtained via peak counts show a slightly larger correlation, increasing of 10% for Gaussian peaks and 20% for starlet, with respect to the power spectrum. We may imagine that having an independent measurement of one of the parameters, it would be of further convenience to use peaks (and starlet filtering) as they increase correlation in the case of (M_ν, Ω_m) and (Ω_m, A_s) . Independently of the correlation, all constraints obtained with starlet filtering

FoM	PS	Gauss Peaks	Gauss Joints	Starlet Peaks	Starlet Joints
M_ν - Ω_m	1222	4259	3666	8899	8831
M_ν - A_s	58	234	202	492	489
Ω_m - A_s	805	3361	2891	7326	7252

TABLE III. Value of the Figure of Merit (FoM) as defined in Equation 21 for each pair of parameters, corresponding to the different observables: the power spectrum alone (PS), the Peaks alone and the two statistics combined (Joints). The figure of merit is inversely proportional to the area of the contours in parameter space: the larger the FoM the smaller the contour. The highest value is given by Starlet Peaks, in all three planes (M_ν, Ω_m), (M_ν, A_s) and (Ω_m, A_s); in all cases the starlet peaks FoM is about twice the one obtained with Gaussian peaks.

FoC	PS	Gaussian Peaks	Gaussian Joints	Starlet Peaks	Starlet Joints
M_ν - Ω_m	1.00	1.22	1.21	1.11	1.11
M_ν - A_s	1.96	1.41	1.41	1.16	1.16
Ω_m - A_s	1.10	1.01	1.00	1.19	1.19

TABLE IV. Value of the Figure of Correlation for each pair of cosmological parameters corresponding to the different tomographic observables: the power spectrum alone (PS), the Peaks alone and the two statistics combined (Joints). As explained in the text, FoC = 1 corresponds to uncorrelated parameters, while the further the FoC is to 1, the more correlations are present. Qualitatively, this can be appreciated by looking at the inclination of the contours: by looking at Figure 6 we can see more ‘oblique’ contours for the Gaussian peaks in the plane (M_ν, Ω_m) compared to the PS or the Starlet peaks, while for the pair (M_ν, A_s) the PS shows more correlation than peaks and for (Ω_m, A_s) Gaussian peaks present slightly smaller correlation than the PS or the Starlet Peaks.

are tighter than the ones obtained via Gaussian filtering, and both are tighter than the ones for the power spectrum.

B. Power spectrum and starlet peak counts

Based on the previous result, we are now interested on the constraints obtained with the starlet filtering. In the right panel of Figure 6 we show the 95% confidence contours corresponding to the power spectrum alone (blue contours), the peaks alone (red contours) and the two statistics combined (we refer to the combination power spectrum and peaks as joints in all Figures, light blue contours). By looking at the contours and at the FoM we find that the joint statistics do not add any relevant information to the peaks alone, leading us to think that the peak counts are a competitive and sufficient statistics for parameter inference when dealing with weak lensing convergence maps as input data. This is confirmed also by the FoC: we obtain the same values for all the pairs of parameters when considering the peaks alone and the joint statistics. We find that this is not specific of the starlet filter: if we consider the same investigation for the Gaussian case, we get very similar values for the FoC of the Joint statistics compared to the peaks alone. This further confirms that lensing peaks are a powerful tool in the context of cosmological parameter inference.

C. Marginalised constraints

In Figure 7 we show the marginalised constraints on each cosmological parameter corresponding to the different observables. To compare the improvement obtained by employing the different statistics we compute the 1σ marginalised error for each parameter, summarised in Table VI. In particular, we find an improvement of 43%, 30% and 60% respectively on M_ν , Ω_m and A_s when employing the Gaussian peaks instead of the power spectrum and an improvement of 71%, 50% and 80% when employing the starlet peaks instead of the power spectrum alone. Namely, the starlet peaks outperform the Gaussian peaks by 50% on M_ν , 25% on Ω_m and 38% on A_s .

D. Starlet scales impact

Figure 8 shows the impact of the different starlet decomposition scales on the constraints. The MCMC chain used for the other results of the analysis has been obtained by considering all starlet scales, i.e. [1.6, 3.2, 6.4] arcmin + *coarse* map, shown in red. To check that we are allowed to exclude the finest scale in the entire analysis, namely not to include the resolution corresponding to 0.8 arcmin - which won’t satisfy the survey requirements - we compare the constraints relative to [0.8, 1.6, 3.2, 6.4] arcmin + *coarse* with the ones for [1.6, 3.2, 6.4] arcmin + *coarse* and we verify that they overlap. We then investigate the impact of the different starlet scales and we

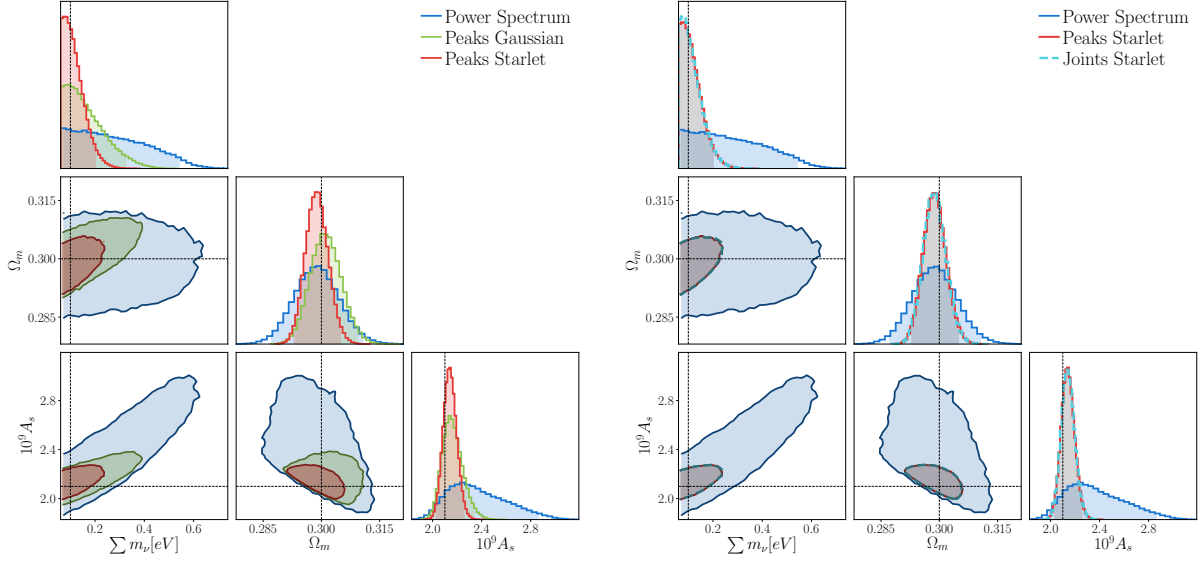


FIG. 6. 95 % confidence contours tomography with redshifts $z = [0.5, 1.0, 1.5, 2.0]$ and corresponding galaxy number density: $n_{\text{gal}} = [11.0159, 11.8906, 5.45201, 1.45283]$. The black dotted line is the fiducial model: $[\sum m_\nu, \Omega_m, 10^9 A_s] = [0.1, 0.3, 2.1]$. **Left panel:** constraints from power spectrum (blue contours) computed on noisy maps smoothed with a Gaussian kernel $\theta_{\text{ker}} = 1$ arcmin, constraints from Gaussian Peak counts (green contours) computed on noisy maps smoothed with a Gaussian kernel $\theta_{\text{ker}} = 1.6$ arcmin, constraints from Starlet Peak counts (red contours) computed on noisy maps smoothed with a Starlet kernel with corresponding resolutions $[1.6, 3.2, 6.4]$ arcmin + coarse map. **Right panel:** constraints from power spectrum (blue contours) computed on noisy maps smoothed with a Gaussian kernel $\theta_{\text{ker}} = 1$ arcmin, constraints from Starlet Peak counts (red contours) computed on noisy maps smoothed with a Starlet kernel with corresponding resolutions $[1.6, 3.2, 6.4]$ arcmin + coarse map and the two statistics joints (light blue contours).

obtain that it is sufficient to consider the setting $[3.2, 6.4]$ + *coarse* map to obtain results competitive with the full set of scales. Hence, we identify 3.2 arcmin as the smallest scale needed to obtain the maximal constraints with convergence maps of resolution 0.4 arcmin. We also perform the inference by using 3.2 arcmin and 6.4 arcmin together and as single scales and we obtain that the only setting that recovers almost the full information is given by $[3.2, 6.4, \text{coarse}]$.

V. CONCLUSIONS

In this paper, we perform inference on the sum of neutrino masses M_ν , the matter density parameter Ω_m and the amplitude of the primordial power spectrum A_s for a survey like *Euclid* with tomographic weak lensing. Our goal is to compare the constraining power of a starlet filter with respect to a Gaussian one in the context of peak counts. We also compute the constraints with standard second-order statistics, in particular using the lensing power spectrum as a benchmark for the comparison. We compare the outcomes obtained from filtering the lensing convergence maps, which have a resolution of 0.4 arcmin with a Gaussian kernel of smoothing size 1.6 arcmin and a starlet kernel. This latter is an isotropic undecimated wavelet transform that allows us to extract the infor-

mation encoded in different scales simultaneously. The starlet scales of a map with a pixel size of 0.4 arcmin correspond to $[0.8, 1.6, 3.2, 6.4]$ arcmin, since the starlet transform returns maps filtered at dyadic scales. We find the following results:

- employing a starlet kernel instead of a Gaussian kernel to filter the noisy maps that we use to compute the peak counts leads to an improvement of twice for the joint constraints on (M_ν, Ω_m) , (M_ν, A_s) and (Ω_m, A_s) . This is even more evident in the marginalised constraints, where the improvement is respectively 50% on M_ν , 25% on Ω_m and 38% on A_s for the comparison between starlet and Gaussian peaks.
- When considering the starlet peaks and the power spectrum we see that the two statistics combined, i.e. using the concatenation of the power spectrum and the peak counts as observables, do not add any relevant information, suggesting that it is sufficient to work with the peaks alone.
- The inclusion of the coarse map when counting peaks preserves crucial information and there exists a minimum resolution (smallest scale needed) for the starlet scales corresponding to $\theta_{\text{ker}} = 3.2$ arcmin for map with a pixel size of 0.4 arcmin to

Observable	M_ν	Ω_m	Ω_m	A_s	A_s
PS alone	0.529	0.288	0.310	2.000	2.886
Peaks Gauss s=1.6	0.326	0.294	0.309	2.018	2.350
PS+Peaks Gauss s=1.6	0.327	0.293	0.309	2.015	2.335
Peaks Gauss s=1.6 diag	0.325	0.293	0.309	2.037	2.322
Peaks Starlet	0.199	0.293	0.305	2.038	2.255
PS+Peaks Starlet	0.199	0.293	0.304	2.039	2.256
Peaks Starlet diag	0.210	0.294	0.305	2.045	2.256
Peaks Starlet [3.2, 6.4, coarse]	0.213	0.293	0.305	2.037	2.266

TABLE V. Values of the 2.5 and 97.5 percentiles for each cosmological parameter as illustrated in Figure 7. In this table we also show the values corresponding to the marginalised constraints obtained using only the diagonal elements of the covariance matrices. They are very similar to the ones obtained by employing the full covariance. This might indicate that the data covariances are almost diagonal. However, a further investigation needs to be done in this direction to check if this result might depend on the employment of the pseudoinverse in the likelihood.

$\sigma_{\alpha\alpha}$	M_ν	Ω_m	A_s
PS alone	0.14	0.006	0.24
Peaks Gauss s=1.6	0.08	0.004	0.08
Peaks Starlet	0.04	0.003	0.05

TABLE VI. Values of 1- σ marginalised error for each cosmological parameter.

get the maximal constraints. This enables us to exclude the first two finest scales of the starlet decomposition, which correspond to the highest frequencies and are the most prone to the impact of noise, allowing for a more efficient and faster analysis.

To summarise, we confirm that weak-lensing peak counts represent a powerful tool when performing inference on cosmological parameters, especially when investigating the non-linear regime where the impact of parameters such as the neutrino masses becomes relevant. We also

point out the importance of adopting tools like the starlet transform, which bring the advantage of analysing the information encoded at different scales simultaneously, thereby leading to better constraints as well as an improvement in terms of efficiency and computation time. We implemented a pipeline that allows us to go from simulated lensing convergence maps as input data to constraints on cosmological parameters as final output, employing different filtering techniques with second-order (the power spectrum) and higher-order statistics (the peak-counts). A future prospect is to generalise the pipeline in terms of flexibility of the input data, to include systematic effects and modelling of the noise, and to ultimately apply it to real data coming from future galaxy surveys.

ACKNOWLEDGMENTS

VA wishes to thank Martin Kilbinger, Santiago Casas, Samuel Farrens, Nicolas Martinet, Niall Jeffrey, José Manuel Zorrilla Matilla, Sebastian Rojas Gonzalez and Inneke Van Nieuwenhuyse for helpful discussions.

-
- [1] J. Lesgourgues and S. Pastor, *Phys. Rep.* **429**, 307 (2006), [arXiv:astro-ph/0603494 \[astro-ph\]](#).
 - [2] A. Peel, F. Lalande, J.-L. Starck, V. Pettorino, J. Merten, C. Giocoli, M. Meneghetti, and M. Baldi, *Phys. Rev. D* **100**, 023508 (2019), [arXiv:1810.11030 \[astro-ph.CO\]](#).
 - [3] S. Hagstotz, M. Gronke, D. F. Mota, and M. Baldi, *A&A* **629**, A46 (2019), [arXiv:1902.01868 \[astro-ph.CO\]](#).
 - [4] J. Merten, C. Giocoli, M. Baldi, M. Meneghetti, A. Peel, F. Lalande, J.-L. Starck, and V. Pettorino, *MNRAS* **487**, 104 (2019), [arXiv:1810.11027 \[astro-ph.CO\]](#).
 - [5] F. Capozzi, E. Lisi, A. Marrone, D. Montanino, and A. Palazzo, *Nuclear Physics B* **908**, 218 (2016), [arXiv:1601.07777 \[hep-ph\]](#).
 - [6] T. Dealtry, *arXiv e-prints*, [arXiv:1904.10206](#) (2019), [arXiv:1904.10206 \[hep-ex\]](#).
 - [7] Planck Collaboration, N. Aghanim, Y. Akrami, M. Ashdown, J. Aumont, C. Baccigalupi, M. Ballardini, A. J. Banday, R. B. Barreiro, N. Bartolo, S. Basak, R. Battye, K. Benabed, J. P. Bernard, Bersanelli, *et al.*, *arXiv e-prints*, [arXiv:1807.06209](#) (2018), [arXiv:1807.06209 \[astro-ph.CO\]](#).
 - [8] R. Laureijs, J. Amiaux, S. Arduini, J. L. Auguères, J. Brinchmann, R. Cole, M. Cropper, C. Dabin, L. Duvet, A. Ealet, B. Garilli, P. Gondoin, L. Guzzo, J. Hoar, and a. o. Hoekstra, *arXiv e-prints*, [arXiv:1110.3193](#) (2011), [arXiv:1110.3193 \[astro-ph.CO\]](#).
 - [9] M. Rizzato, K. Benabed, F. Bernardeau, and F. Lacasa, *arXiv e-prints*, [arXiv:1812.07437](#) (2018),

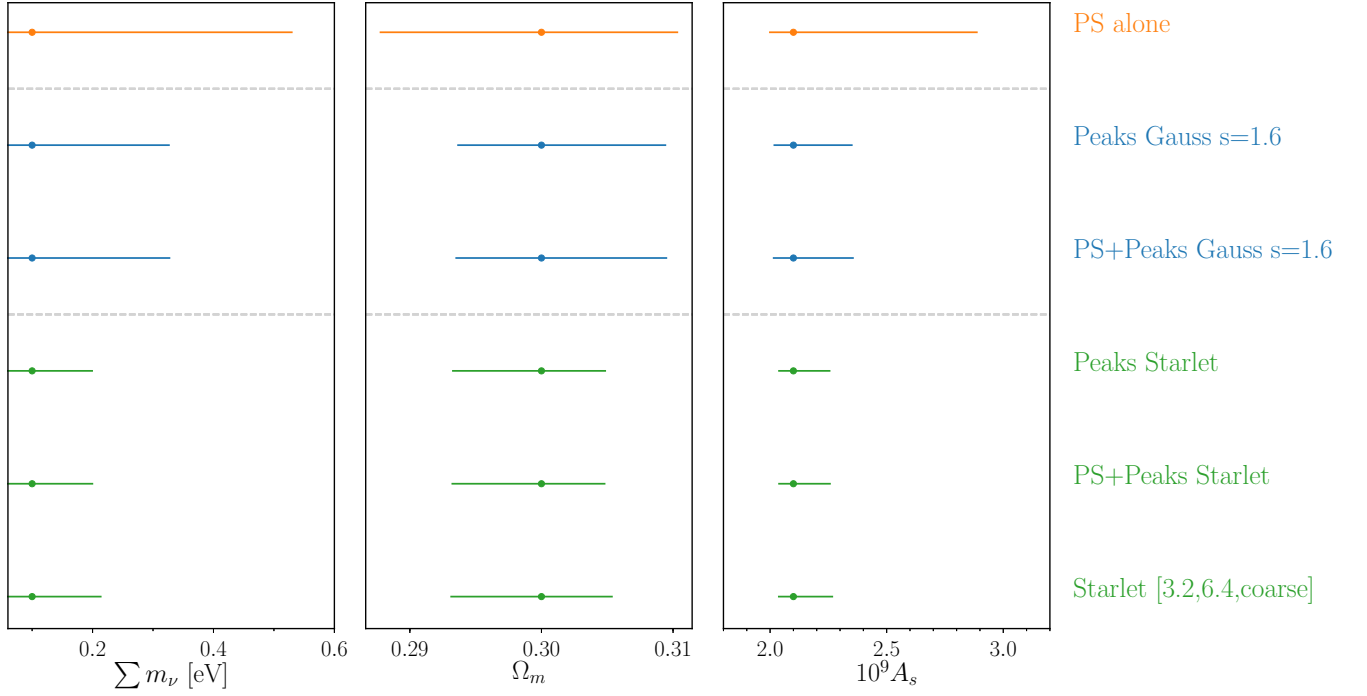


FIG. 7. Marginalized constraints on each parameter for forecasts showing the 2.5 and 97.5 percentiles with respect to the fiducial model. These marginalised constraints refer to a tomographic setting with $z = [0.5, 1.0, 1.5, 2.0, 2.5]$ with the fiducial model set at $[M_\nu, \Omega_m, 10^9 A_s] = [0.1, 0.3, 2.1]$ corresponding to the different observables employed within the likelihood analysis.

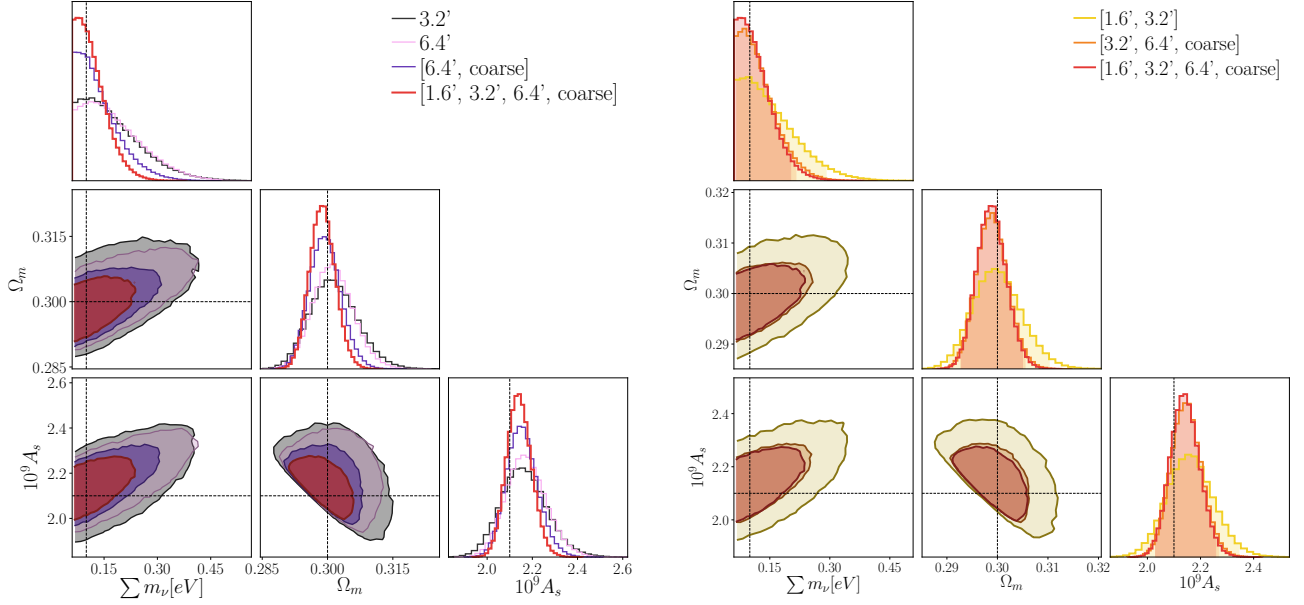


FIG. 8. 95 % confidence contours using tomography with redshifts $z = [0.5, 1.0, 1.5, 2.0]$ and corresponding galaxy number densities $n_{\text{gal}} = [11.0159, 11.8906, 5.45201, 1.45283]$. The black dotted line is the fiducial model: $[\sum m_\nu, \Omega_m, 10^9 A_s] = [0.1, 0.3, 2.1]$. We show the impact of the different starlet scales and we prove there exists a minimum resolution $\theta_{\text{ker}} = 3.2$ arcmin that allows us to obtain constraints comparable to what is achieved with the full wavelet decomposition and that the information contained in the coarse map cannot be neglected. **Left panel:** Constraints corresponding to 3.2 arcmin without the coarse map are shown in black, the ones coming from 6.4 arcmin in pink, the ones coming from 6.4 arcmin + coarse in violet and the full wavelet decomposition as taken into account in this paper in red. **Right panel:** The constraints corresponding to [1.6, 3.2] arcmin without the coarse map are shown in yellow, the ones coming from [3.2, 6.4] arcmin + coarse in orange and the full wavelet decomposition as taken into account in this paper in red.

- arXiv:1812.07437 [astro-ph.CO].
- [10] I. Kayo and M. Takada, arXiv e-prints, arXiv:1306.4684 (2013), arXiv:1306.4684 [astro-ph.CO].
 - [11] A. Petri, Z. Haiman, L. Hui, M. May, and J. M. Kratochvil, *Phys. Rev. D* **88**, 123002 (2013), arXiv:1309.4460 [astro-ph.CO].
 - [12] J. M. Kratochvil, E. A. Lim, S. Wang, Z. Haiman, M. May, and K. Hufenberger, *Phys. Rev. D* **85**, 103513 (2012), arXiv:1109.6334 [astro-ph.CO].
 - [13] T. Kacprzak, D. Kirk, O. Friedrich, A. Amara, A. Refregier, L. Marian, J. P. Dietrich, E. Suchyta, J. Aleksić, D. Bacon, M. R. Becker, C. Bonnett, S. L. Bridle, C. Chang, Y. Eifler, and others, and DES Collaboration, *MNRAS* **463**, 3653 (2016), arXiv:1603.05040 [astro-ph.CO].
 - [14] C.-A. Lin and M. Kilbinger, *A&A* **583**, A70 (2015), arXiv:1506.01076 [astro-ph.CO].
 - [15] A. Peel, C.-A. Lin, F. Lanusse, A. Leonard, J.-L. Starck, and M. Kilbinger, *A&A* **599**, A79 (2017), arXiv:1612.02264 [astro-ph.CO].
 - [16] N. Martinet, J. G. Bartlett, A. Kiessling, and B. Sartoris, *A&A* **581**, A101 (2015), arXiv:1506.02192 [astro-ph.CO].
 - [17] H. Shan, X. Liu, H. Hildebrandt, C. Pan, N. Martinet, Z. Fan, P. Schneider, M. Asgari, J. Harnois-Déraps, H. Hoekstra, A. Wright, J. P. Dietrich, T. Erben, F. Getman, A. Grado, C. Heymans, D. Klaes, K. Kuijken, J. Merten, E. Puddu, M. Radovich, and Q. Wang, *MNRAS* **474**, 1116 (2018), arXiv:1709.07651 [astro-ph.CO].
 - [18] N. Martinet, P. Schneider, H. Hildebrandt, H. Shan, M. Asgari, J. P. Dietrich, J. Harnois-Déraps, T. Erben, A. Grado, C. Heymans, H. Hoekstra, D. Klaes, K. Kuijken, J. Merten, and R. Nakajima, *MNRAS* **474**, 712 (2018), arXiv:1709.07678 [astro-ph.CO].
 - [19] A. Petri, *Astronomy and Computing* **17**, 73 (2016), arXiv:1606.01903 [astro-ph.CO].
 - [20] J. Liu, S. Bird, J. M. Zorrilla Matilla, J. C. Hill, Z. Haiman, M. S. Madhavacheril, A. Petri, and D. N. Spergel, *JCAP* **2018**, 049 (2018), arXiv:1711.10524 [astro-ph.CO].
 - [21] J. Liu and M. S. Madhavacheril, *Phys. Rev. D* **99**, 083508 (2019), arXiv:1809.10747 [astro-ph.CO].
 - [22] G. A. Marques, J. Liu, J. M. Zorrilla Matilla, Z. Haiman, A. Bernui, and C. P. Novaes, *JCAP* **2019**, 019 (2019), arXiv:1812.08206 [astro-ph.CO].
 - [23] W. R. Coulton, J. Liu, M. S. Madhavacheril, V. Böhm, and D. N. Spergel, *JCAP* **2019**, 043 (2019), arXiv:1810.02374 [astro-ph.CO].
 - [24] LSST Science Collaboration, P. A. Abell, J. Allison, S. F. Anderson, J. R. Andrew, J. R. P. Angel, L. Armus, D. Arnett, S. J. Asztalos, T. S. Axelrod, S. Bailey, D. R. Balantyne, J. R. Bankert, W. A. Barkhouse, J. D. Barr, L. F. Barrientos, A. J. Barth, Bartlett, *et al.*, arXiv e-prints, arXiv:0912.0201 (2009), arXiv:0912.0201 [astro-ph.IM].
 - [25] Z. Li, J. Liu, J. M. Z. Matilla, and W. R. Coulton, *Phys. Rev. D* **99**, 063527 (2019), arXiv:1810.01781 [astro-ph.CO].

- ph.CO].
- [26] J.-L. Starck, F. Murtagh, and J. Fadili, *Sparse Image and Signal Processing: Wavelets, Curvelets, Morphological Diversity* (Cambridge University Press, New York, NY, USA, 2010).
 - [27] C.-A. Lin, M. Kilbinger, and S. Pires, *A&A* **593**, A88 (2016), [arXiv:1603.06773 \[astro-ph.CO\]](#).
 - [28] M. Kilbinger, *Reports on Progress in Physics* **78**, 086901 (2015), [arXiv:1411.0115 \[astro-ph.CO\]](#).
 - [29] P. Schneider, J. Ehlers, and E. E. Falco, *Gravitational Lenses* (1992).
 - [30] N. Kaiser and G. Squires, *ApJ* **404**, 441 (1993).
 - [31] Euclid Collaboration, A. Blanchard, S. Camera, C. Carbone, V. F. Cardone, S. Casas, S. Ilić, M. Kilbinger, T. Kitching, M. Kunz, F. Lacasa, E. Linder, E. Majerotto, K. Marković, M. Martinelli, V. Pettorino, *et al.*, [arXiv e-prints](#), [arXiv:1910.09273](#) (2019), [arXiv:1910.09273 \[astro-ph.CO\]](#).
 - [32] W. R. Coulton, J. Liu, I. G. McCarthy, and K. Osato, (2019), [arXiv:1910.04171 \[astro-ph.CO\]](#).
 - [33] J.-L. Starck, J. Fadili, and F. Murtagh, *IEEE Transactions on Image Processing* **16**, 297 (2007).
 - [34] J.-L. Starck, F. D. Murtagh, and A. Bijaoui, “The wavelet transform,” in *Image Processing and Data Analysis: The Multiscale Approach* (Cambridge University Press, 1998) p. 145.
 - [35] A. Peel, V. Pettorino, C. Giocoli, J.-L. Starck, and M. Baldi, *A&A* **619**, A38 (2018), [arXiv:1805.05146 \[astro-ph.CO\]](#).
 - [36] M. J. Jee, J. A. Tyson, M. D. Schneider, D. Wittman, S. Schmidt, and S. Hilbert, *ApJ* **765**, 74 (2013), [arXiv:1210.2732 \[astro-ph.CO\]](#).
 - [37] T. Abbott, F. B. Abdalla, S. Allam, A. Amara, J. Annis, R. Armstrong, D. Bacon, M. Banerji, A. H. Bauer, E. Baxter, M. R. Becker, A. Benoit-Lévy, R. A. Bernstein, Bernstein, J. others, and Dark Energy Survey Collaboration, *Phys. Rev. D* **94**, 022001 (2016), [arXiv:1507.05552 \[astro-ph.CO\]](#).
 - [38] H. Hildebrandt, M. Viola, C. Heymans, S. Joudaki, K. Kuijken, C. Blake, T. Erben, B. Joachimi, D. Klaes, L. Miller, C. B. Morrison, R. Nakajima, G. Verdoes Kleijn, A. Amon, Choi, *et al.*, *MNRAS* **465**, 1454 (2017), [arXiv:1606.05338 \[astro-ph.CO\]](#).
 - [39] J.-L. Starck and F. Murtagh, *PASP* **110**, 193 (1998).
 - [40] C. E. Rasmussen and C. K. I. Williams, *Gaussian Processes for Machine Learning (Adaptive Computation and Machine Learning)* (The MIT Press, 2005).
 - [41] J. Carron, *A&A* **551**, A88 (2013), [arXiv:1204.4724 \[astro-ph.CO\]](#).
 - [42] J. Hartlap, P. Simon, and P. Schneider, *A&A* **464**, 399 (2007), [arXiv:astro-ph/0608064 \[astro-ph\]](#).
 - [43] E. Sellentin and A. F. Heavens, *MNRAS* **456**, L132 (2016), [arXiv:1511.05969 \[astro-ph.CO\]](#).
 - [44] E. Sellentin and A. F. Heavens, *MNRAS* **464**, 4658 (2017), [arXiv:1609.00504 \[astro-ph.CO\]](#).
 - [45] S. Casas, M. Kunz, M. Martinelli, and V. Pettorino, *Physics of the Dark Universe* **18**, 73 (2017), [arXiv:1703.01271 \[astro-ph.CO\]](#).
 - [46] D. Foreman-Mackey, D. W. Hogg, D. Lang, and J. Goodman, *PASP* **125**, 306 (2013), [arXiv:1202.3665 \[astro-ph.IM\]](#).
 - [47] S. R. Hinton, *The Journal of Open Source Software* **1**, 00045 (2016).